Supporting Information

for

Enhancing Long-Range Energy Transport in Supramolecular Architectures by Tailoring Coherence Properties

Bernd Wittmann[1], Felix A. Wenzel[2,3], Stephan Wiesneth[1], Andreas T. Haedler[2,3], Markus Drechsler[4], Klaus Kreger[2], Jürgen Köhler[1], E. W. Meijer[3], Hans-Werner Schmidt*[2], Richard Hildner*[1,5]

Affiliations:

[1]Spectroscopy of Soft Matter, University of Bayreuth, Universitätsstraße 30, 95447 Bayreuth, Germany.

[2]Macromolecular Chemistry and Bavarian Polymer Institute, University of Bayreuth, Universitätsstraße 30, 95447 Bayreuth, Germany.

[3]Institute for Complex Molecular Systems, Laboratory of Macromolecular and Organic Chemistry, Eindhoven University of Technology, 5612 AZ Eindhoven, The Netherlands.

[4]Bavarian Polymer Institute, University of Bayreuth, Universitätsstraße 30, 95447 Bayreuth, Germany.

[5]Zernike Institute for Advanced Materials, University of Groningen, Nijenborgh 4, 9747 AG Groningen, The Netherlands.

*Correspondence to: r.m.hildner@rug.nl and hans-werner.schmidt@uni-bayreuth.de.

Table of Content

1. Materials and Methods

Materials. The synthesis, purification and characterization of compound **1** is described in detail elsewhere [1]. All solvents were of HPLC grade and used as received.

*Molecularly dissolved solution of compound **1**.* A 40 µM solution of compound **1** in THF (boiling point: 66 °C) was refluxed for 20 minutes under stirring and allowed to cool to room temperature.

*Self-assembly of compound **1**.* Compound **1** was added at a concentration of 40 µM (~100 p.p.m., 0.01 wt%) in n-dodecane (bp.: 216 °C) or anisole (bp.: 154 °C), respectively. A homogeneous dispersion was ensured by ultrasonication for 15 minutes. The dispersions were refluxed for 30 minutes under stirring and then allowed to cool to room temperature. The self-assembly process was monitored via UV/vis and PL spectroscopy until no spectral changes were detected. Subsequently, all samples were stored for 24 hours prior investigation.

AFM. For AFM measurements, we used silicon wafers as substrate. The self-assembled 40 µM dispersions were either spin-coated directly or spin-coated after dilution to a concentration of 4 µM. All samples were dried under vacuum. AFM images were recorded on a Dimension 3100 NanoScope V (Veeco Metrology Group). Scanning was performed in tapping mode using silicon nitride (Si_3N_4) cantilevers (OTESPA-R3, Bruker) with a typical spring constant of 26 N m^{-1} and a typical resonance frequency of 300 kHz. Image processing and analysis was conducted with the Gwyddion 2.52 software.

TEM and SAED. The self-assembled 40 µM dispersions were drop-cast on a carbon-coated copper grid and the solvent was removed with a filter paper. Finally, all samples were dried under vacuum. TEM images were recorded with a Zeiss / LEO EM922 Omega and a JEOL JEM-2200FS energy filtering transmission electron microscope (EFTEM) both operated at 200 kV in bright-field and diffraction mode. Zero-loss filtered micrographs ($\Delta E \sim 0$ eV) were recorded with bottom mounted camera systems. The Zeiss microscope was equipped with a CCD camera system (Ultrascan 1000, Gatan) and the JEOL microscope with a CMOS camera system (OneView, Gatan). Both camera systems were operated with an image acquisition and processing software (Digital Micrograph GMS 1.9 resp. 3.3).

UV/vis, photoluminescence and circular dichroism spectroscopy in solution. UV/vis absorption spectra were recorded on a Perkin Elmer Lambda750 spectrophotometer. Photoluminescence (PL) spectra were measured on a Varian Cary Eclipse at excitation wavelengths of 430 nm for n-dodecane dispersions and THF solutions and 380 nm for anisole dispersions. All PL spectra were corrected for reabsorption with the factor $\boldsymbol{k_{abs} = 10^{0.5\,OD(\lambda)}}$, where $\boldsymbol{OD(\lambda)}$ is the wavelength dependent absorbance. The PL quantum efficiency was measured on a JASCO FP-8600 spectrofluorometer equipped with an integrating sphere (ILF-835). Circular dichroism spectra were recorded on a Jasco J-715 spectrophotometer. All measurements were conducted with Hellma QS quartz-glass cuvettes.

Optical imaging and spectroscopy of single supramolecular nanofibres and bundles. The 40 µM-dispersions were either diluted to 4 µM before spin-coating, or spin-coated undiluted on microscopy cover slips (borosilicate glass; thickness 0.17 µm; Carl Roth). All samples were dried under vacuum. Optical imaging and spectroscopy was performed using a home-built microscope (Fig. S11). The excitation source was a pulsed diode laser (LDH-P-C-450B, Picoquant; 2.5 MHz repetition rate, 70 ps pulse duration) that operates at a wavelength of 450 nm. The laser light was spatially filtered and directed to the microscope, which was equipped

with an infinity-corrected high-numerical aperture oil-immersion objective (PlanApo, 60×, numerical aperture 1.45; Olympus). The sample was placed in the focal plane of the objective, and the sample position was controlled by a piezo-stage (Tritor 102 SG, from piezosystem jena). Photoluminescence was collected by the same objective and passed a set of dielectric filters (dichroic beam splitter z460RDC, long-pass filter LP467; AHF Analysentechnik) to suppress scattered or reflected laser light.

The detection beam path is equipped with a closed-loop piezo scan mirror (S-335.2.SH, PI) and a single-photon-counting avalanche photodiode (MPD, Picoquant) to position the detection spot independently from the confocal excitation spot (Fig. S11). The electrical signal of the photodiode was fed into a time-correlated single-photon-counting module (TimeHarp 260 PICO, Picoquant).

In imaging mode, the photoluminescence signal was imaged onto a CMOS camera (Zyla 4.2 sCMOS, Andor). In this mode, we used two illumination methods. First, for widefield illumination we flipped an additional lens (widefield lens) into the excitation beam path to focus the laser light into the back-focal plane of the microscope objective. This allows for nearly uniform illumination of a large area with ∼70 µm diameter in the sample plane, to acquire overview PL images of our samples and to identify elongated nanostructures (Fig. 4A and 4B). Second, for confocal illumination the widefield lens was removed and the laser light was tightly focused to a spot with a half width at half maximum of ∼170 nm in the sample plane. A flip-mirror allows to switch between imaging and single-photon counting mode of the setup.

For measurements on single supramolecular nanofibres and bundles, the excitation intensities were below 140 W cm^{-2} for confocal illumination and 1.3 W cm^{-2} for widefield illumination These intensities correspond to a maximum excitation probability of 0.1 absorbed photon per pulse per 3000 CBT-cores along a column and confirm that our experiments are conducted in a regime where annihilation does not play a role. All experiments were carried out at room temperature under ambient conditions.

Numerical Simulations. For the numerical simulation of the absorption and PL spectra shown in Fig. 3B,C we used home-written Matlab-scripts. The electronic Coulomb coupling between CBT-cores along a column was treated in nearest-neighbour approximation. The transition energies of the CBT-cores were taken from a Gaussian distribution with width σ. To account for different degrees of intra-column electronic disorder, a correlation length l_0 was introduced, i.e., with increasing l_0, the distribution of transition energies within a column becomes smoother (see Fig. 3D). To model the experimental spectra we averaged over 10^4 realisations of electronic disorder and performed a residual analysis. Further details are outlined in the Supplementary Materials, Fig. S9 and S10 and section 5.

2. Characterisation of Supramolecular Architectures of Compound 1

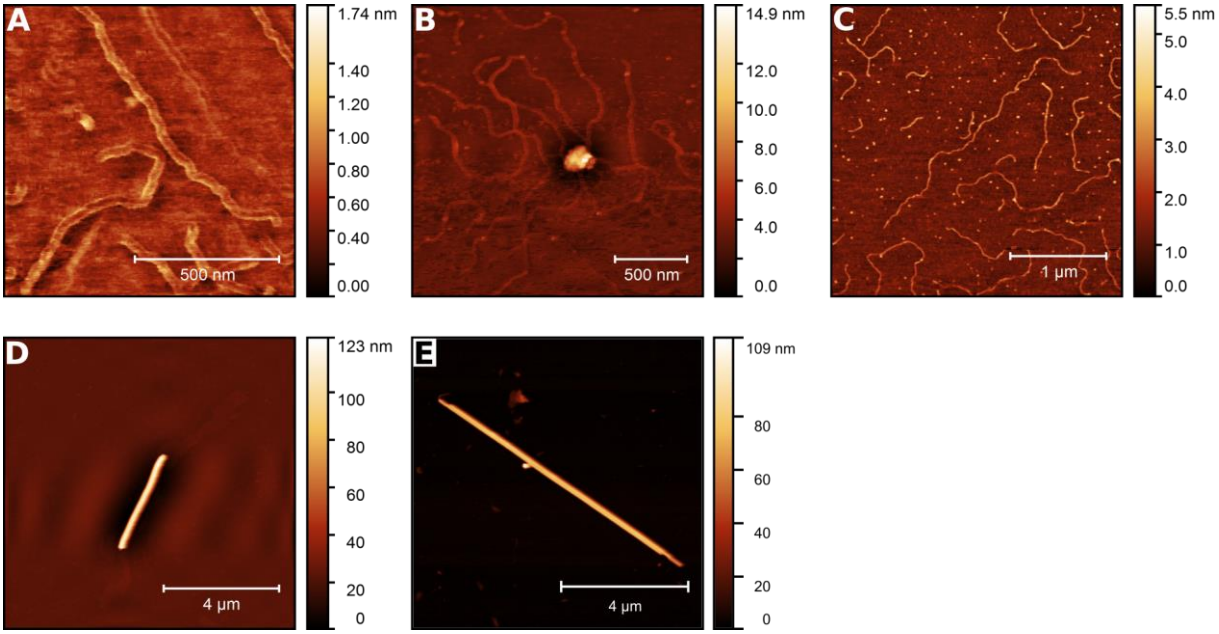

Fig. S1: AFM images of single supramolecular nanofibres and bundles of nanofibres. A-C) AFM images (topographical scan) of single nanofibres spin-coated from a dispersion of compound **1** in n-dodecane (**A,B**: 40 µM; **C**: 4 µM) demonstrating the presence of single nanofibres at concentrations of 4 µM as well as of 40 µM. The discrepancy between the heights and the diameters of the nanofibres, as determined by AFM (2–2.5 nm) and molecular modelling (4.4 nm) [2], respectively, is a known phenomenon [3,4]. **D,E)** AFM images (topographical scan) of bundles of nanofibres spin-coated from a dispersion of compound **1** in anisole at a concentration of 40 µM.

3. Selected Area Electron Diffraction of Bundles of Supramolecular Nanofibres

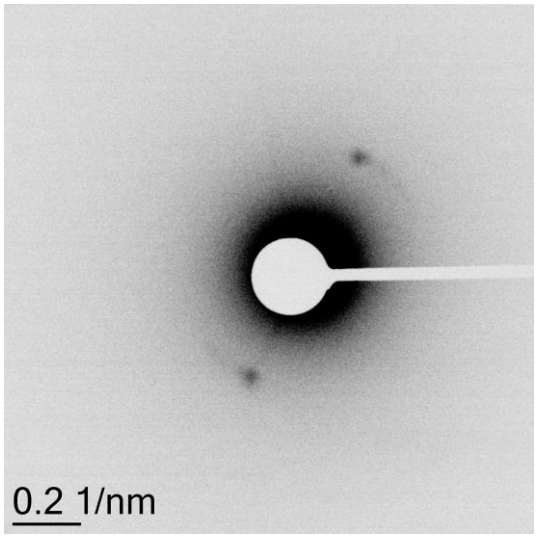

Fig. S2: Selected Area Electron Diffraction (SAED) at smaller angles. SAED pattern from a sample as in Fig. 2G (prepared from a dispersion of self-assembled compound **1** in anisole, concentration 40 µM), which reveals sharp signals corresponding to a distance of 2.8 nm. Assuming a columnar hexagonal packing of nanofibres within bundles [1], this plane-plane distance corresponds to an intercolumnar spacing of 3.23 nm.

4. Optical Spectroscopy and Spectroscopic Characteristics of H-Aggregates

Franck-Condon Analysis of Absorption and PL Spectra

For the Franck-Condon analysis of the PL and absorption spectra of molecularly dissolved compound **1** in THF (Fig. 3A) we assume coupling of the electronic transition to a single effective vibrational mode (carbon-bond stretch). In this situation, the normalized spectra for PL $I_{PL}(\omega)$ and for absorption $I_{Abs}(\omega)$ can be described by [5]

$$\frac{I_{PL}(\omega)}{n^3\omega^3} \propto \sum_m \frac{S^m}{m!} e^{-S} \Gamma[\omega - (\omega_{0-0} - m\omega_0)] \qquad (1)$$

$$\frac{I_{Abs}(\omega)}{n\omega} \propto \sum_m \frac{S^m}{m!} e^{-S} \Gamma[\omega - (\omega_{0-0} + m\omega_0)] \qquad (2)$$

Here S is the Huang–Rhys factor for the effective vibrational mode with energy ω_0, $\omega_{0\text{-}0}$ is the energy of the purely electronic 0–0 transition, $m = (1,2, \dots)$ denotes the vibrational quantum number and n is the refractive index. Γ is the Gaussian (inhomogeneous) line width function with a standard deviation σ, which we allow to be different for the electronic and vibronic transitions (the effective mode is typically a superposition of several modes that are closely spaced and that give rise to a larger "effective" inhomogeneous line width for the ensemble vibronic transition).

To describe both the absorption and the PL with the same Huang-Rhys factor S and vibrational energy ω_0, we fit absorption and PL simultaneously. The parameters for the best fit are shown in Tab. S1.

Tab. S1: Franck-Condon analysis of the absorption and PL spectra of molecularly dissolved compound 1 in THF.

	S	ω_{0-0}/eV	ω_0/eV	σ_{0-0}/eV	$\sigma_{0-1,2..}/eV$
Abs.	0.54 ± 0.02	2.664 ± 0.003	0.157 ± 0.005	0.090 ± 0.002	0.133 ± 0.008
PL	0.54 ± 0.02	2.544 ± 0.003	0.157 ± 0.005	0.082 ± 0.003	0.105 ± 0.008

Concentration-Dependent Absorption Spectra of Compound 1 in Anisole

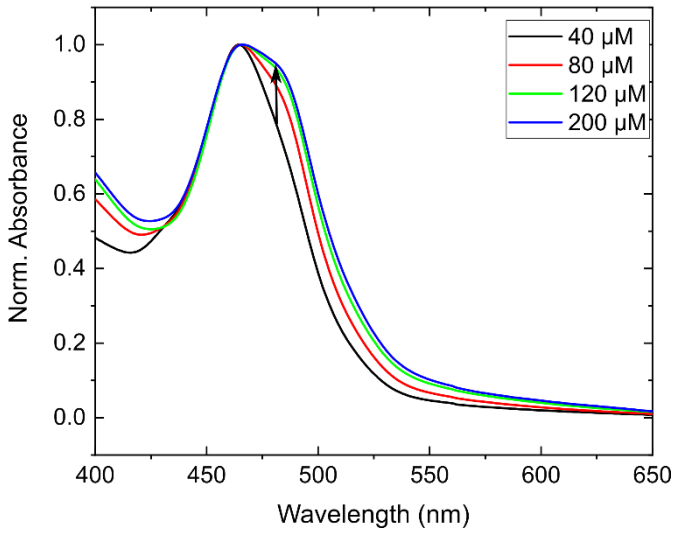

Fig. S3: Concentration-dependent absorption spectra of compound 1 in anisole. Due to the remaining solubility of compound **1** at low concentrations (40 µM, black) in anisole, the absorption is a superposition of the absorption of molecularly dissolved compound **1** and of bundles of nanofibres. We therefore increased the concentration until no further spectral changes occurred (at 200 µM, blue), i.e., mainly bundles of nanofibres exist in the anisole dispersion.

Circular-Dichroism Spectroscopy

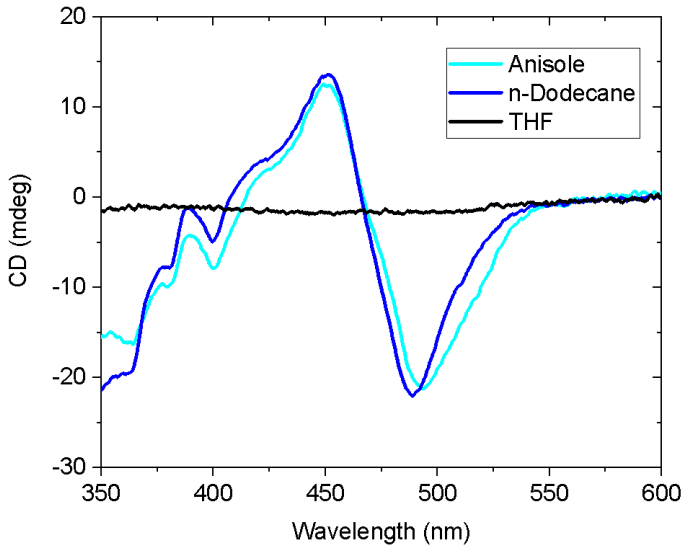

Fig. S4: Circular dichroism spectroscopy of compound 1. Circular dichroism spectra of compound **1** in THF (molecularly dissolved, black), n-dodecane (single supramolecular nanofibres, blue) and anisole (bundles of supramolecular nanofibres, cyan), each recorded at a concentration of about 40 µM (~100 ppm) at room temperature. While there is no circular-dichroism signal for the molecularly dissolved building block in THF, aggregates formed in n-dodecane and anisole exhibit a nearly identical circular-dichroism activity, which suggests a comparable structural arrangement within the columns of the supramolecular aggregates [6].

Optical Absorption and PL Spectra of Molecular Aggregates

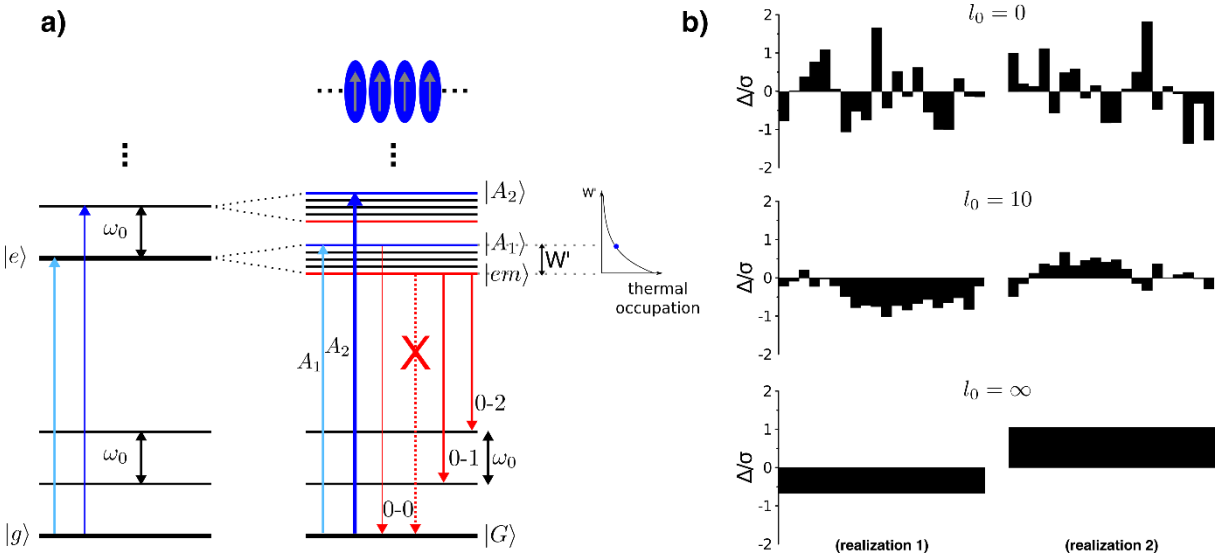

Fig. S5: Spano model of H-type assemblies. a) Left: Energy level scheme for a molecule with an intra-molecular vibrational mode of energy w_0, coupling to the electronic transition between electronic ground $|g\rangle$ and excited electronic state $|e\rangle$. Right: Upon electronic Coulomb coupling between molecules a progression of vibronic exciton bands is formed, separated in energy by the vibrational energy w_0 and with an exciton bandwidth W'. The optically accessible exciton states, labelled $|A_1\rangle, |A_2\rangle, ...$, are located at the top of each band (blue solid lines), while emission occurs only from the lowest-energy exciton state $|em\rangle$ (red solid line). In a perfect H-aggregate the 0-0 transition from $|em\rangle$ into the ground state $|G\rangle$ is optically forbidden, while the 0-1, 0-2, … transitions are still allowed. Thermal energy populates (optically allowed) higher-energy exciton states in the lowest-energy exciton band. Hence, with increasing temperature an increasing intensity of the 0-0 PL intensity is observed. Solid coloured arrows indicate the allowed optical transitions [7,8]. **b)** Six realisations of correlated site-energy disorder along an aggregate. Left and right column depict two different realisations of transition energy offsets Δ_n of an aggregate consisting of N=20 monomers for three correlation lengths l_0 (increasing from the top to the bottom) [7,9].

The optical spectra of organic molecules show a pronounced vibronic progression (Fig. 3A). This electron-phonon coupling of intra-molecular vibrations (typically carbon-bond stretch modes with energies $\omega_0 \approx 1400 - 1600\ cm^{-1}$) to electronic transitions is characterised by the Huang-Rhys parameter *S*. In the simplest picture, each molecule is described as a two level system, which couples to one (effective) intra-molecular vibration with the vibrational energy ω_0 (Fig. S5a, left).

If organic molecules are densely assembled in an aggregate, their transition dipole moments interact via electronic Coulomb coupling J_0 (in nearest-neighbour approximation). To include the influence of electron-phonon coupling on the aggregate spectra, Spano *et al.* [6–9] introduced one- and two-particle states. A one-particle state $|n, \tilde{v}\rangle$ consist of one vibronically excited molecule n, i.e., molecule n is in its electronically excited state with $\tilde{v} \geq 0$ vibrational quanta, and all other molecules of the aggregate are in their vibrationless electronic ground state. For two-particle states $|n, \tilde{v}, n', v'\rangle$, in addition to the vibronic excitation of molecule n, molecule $n'(\neq n)$ is in a vibrational excited state $v' \geq 1$ of its electronic ground state. The αth eigenstate of the aggregate can then be written as a superposition of one- and two-particle states,

$$|\Psi^{\alpha}\rangle = \sum_{n,\tilde{\nu}} c^{\alpha}_{n,\tilde{\nu}} \ |n,\tilde{\nu}\rangle + \sum_{n,\tilde{\nu}} \sum_{n',\nu'} c^{\alpha}_{n,\tilde{\nu},n',\nu'} \ |n,\tilde{\nu},n',\nu'\rangle, \qquad (3)$$

where the wave function coefficients c_j^i are obtained via diagonalization of the Hamiltonian of the system.

Now a series of vibronic exciton bands form (Fig. S5a, right) that feature a reduced bandwidth W' compared to the free exciton bandwidth $W = 4|J_0|$ due to electron-phonon coupling. In perfect, disorder-free systems, vibronic excitons are delocalised over the entire aggregate. For H-aggregates only transitions from the ground state to the highest-energy exciton of each band are allowed. These optically accessible states are labelled $|A_{i+1}\rangle$ $(i = 0,1, \dots)$ and correlate to the $0-i$ transitions of the isolated molecule (Fig. S5 a). Consequently, the optically accessible vibronic exciton states show up as a progression of peaks with an energy difference of ω_0 in the absorption spectrum. Furthermore, as the coupling J_0 rises, the oscillator strength is increasingly redistributed towards higher energy bands (e.g. from $|A_1\rangle \ to, |A_2\rangle, \dots$), leading to a decreased $|A_1\rangle$ intensity compared to the monomer 0-0-intensity in absorption. Hence, the relative intensity of the $|A_1\rangle$ absorption is a direct measure for the magnitude of the electronic Coulomb coupling.

PL takes place from the lowest-energy exciton state $|em\rangle$ of the lowest-energy vibronic exciton band. Absence of disorder leads to a highly symmetric exciton wave function for this state with alternating sign of wavefunction coefficients between consecutive monomers, leading to destructive interference of the 0-0-intensity compared to the monomer PL spectrum. Hence, in ideal H-aggregates the 0-0-peak in emission is completely suppressed, while the remaining progression (0-1, 0-2, etc.) is still visible, because momentum conservation is satisfied by simultaneously exciting a vibration in the electronic ground state.

If PL spectra are recorded at temperatures $T \neq 0$K, states above the lowest-energy exciton state become thermally accessible (thermally activated emission), i.e., PL stems no longer exclusively from the lowest-energy exciton state $|em\rangle$. For ideal H-aggregates, increasing temperature thus leads to an enhanced 0-0 PL intensity. As the bandwidth W' of the lowest-energy exciton band rises, thermal occupation of higher-energy exciton states becomes less likely (for a given temperature, see Fig. S5a, right, thermal occupation of states), i.e., the 0-0 PL intensity is determined by the ratio between the thermal energy and the exciton bandwidth W.

Until now we considered disorder-free aggregates with excitons being delocalised over the entire aggregate ($N_{coh} = N$, N_{coh} is the number of coherently coupled molecules). In real aggregates, structural and electronic disorder is present, which localises excitons ($N_{coh} < N$).

Because of electronic disorder, the transition energies of the individual molecules of the aggregate are distributed around an average transition energy ϵ_0. For a description of this distribution, the individual transition energy offsets Δ_n are chosen from a joint Gaussian distribution [9]

$$P(\Delta_1, \dots, \Delta_N) = \left[\frac{1}{\sqrt{2\pi}}\right]^N \frac{1}{\sqrt{det\ A}} exp[-0.5 \sum_{n.m=1} (A^{-1})_{nm} \Delta_n \Delta_m \ ] \qquad (4)$$

where $(A^{-1})_{nm}$ are the elements of the inverse of the covariance matrix A. The matrix elements are given by

$$A_{nm} = \sigma^2 e^{-\frac{|n-m|}{l_0}}, \qquad (5)$$

where σ is a measure for the disorder strength, defined as $\sigma \equiv \sqrt{\langle \Delta_n^2 \rangle}$ ($\langle \dots \rangle$ denotes the mean over all realizations). l_0 describes the spatial correlation of transition energies in units of monomers. For $l_0 = 0$ each transition energy offset Δ_n is chosen independently from a Gaussian distribution. In the opposite limit of infinite spatial correlation ($l_0 = \infty$) each monomer within one aggregate exhibits the same energy and disorder is entirely inter-aggregate, see Fig. S5b. By means of correlated energy disorder, inter-aggregate (disorder between aggregates, parameter σ) as well as intra-aggregate electronic disorder (within one aggregate, parameter l_0) is taken into account.

Qualitatively, at $T = 0K$ and for increasing disorder (increasing σ and/or decreasing l_0) the 0-0 PL intensity increases, due to the broken symmetry in the exciton wave function. Moreover, the 0-0 PL intensity is a strong function of N_{coh}, in contrast to the sideband PL 0-1, 0-2, etc. [9]. Therefore, the 0-0 PL-intensity reports on the degree of coherence of the emitting exciton, in particular, the number of coherently coupled molecules N_{coh} can be determined from

$$N_{coh} \equiv \frac{1}{\langle C^{em}(0) \rangle} \sum_{s=-(N-1)}^{N-1} |\langle C^{em}(s) \rangle| . \quad (6)$$

Here, the coherence function for the emitting exciton $|em\rangle$, i.e., the delocalisation of the vibronically excited centre of mass of the exciton, is defined as [9]

$$C^{em}(s) = \sum_n \sum_{\tilde{\nu},\tilde{\nu}'} f_{\tilde{\nu},0}\, f_{\tilde{\nu}',0}\, c^{em}_{n,\tilde{\nu}}\, c^{em}_{n+s,\tilde{\nu}'}, \quad (7)$$

where $f_{\tilde{\nu},\nu}$ are the vibrational overlap factors, $c^{em}_{n,\tilde{\nu}}$ are the one-particle coefficients and n counts the monomers along the aggregate.

For example, for aggregates without disorder ($\sigma = 0\ and/or\ l_0 = \infty$) and periodic boundary conditions $N_{coh} = N$.

Note that motional narrowing should be in principle observable in our data. However, motional narrowing affects mainly the 0-0 PL peak line width, which is largely suppressed in our supramolecular nanofibres. Also the probability of the presence of energetically low-lying states in an aggregate decreases with increasing correlation length l_0 [9]. Consequently, the linewidths in emission decrease only slightly with increasing size of the aggregates.

Temperature-Dependent PL Spectroscopy of Compound 1 in n-Dodecane

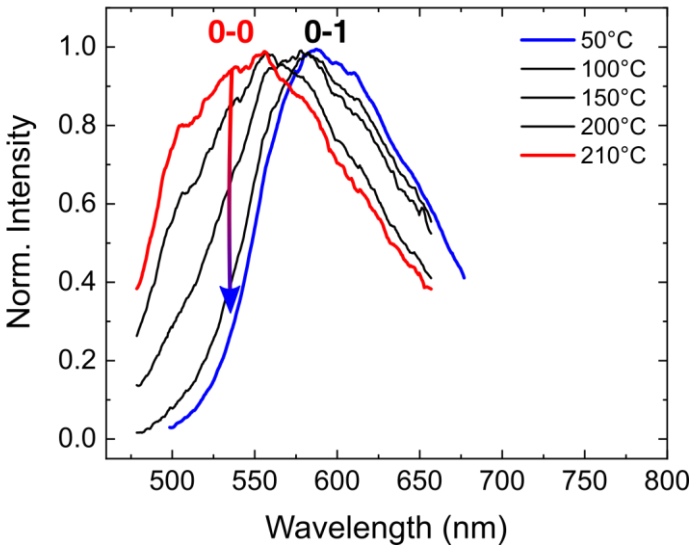

Fig. S6: Temperature-dependent PL spectra of compound 1 in n-dodecane. To support our assignment of the 0-0 and 0-1-peak in the PL spectrum taken from a dispersion of compound **1** in n-dodecane at room temperature (Fig. 3B), we performed temperature dependent PL-spectroscopy on this dispersion. Upon cooling from 210 °C to room temperature, the 0-0 peak decreases continuously. For these measurements, the dispersions are filled in Hellma QS quartz-glass cuvettes at a concentration of 40 µM (100 ppm). The cuvettes were placed inside an aluminium block on a heating plate. The excitation source was a continuous-wave laser that operates at a wavelength of 405 nm. The PL passed a dielectric filter (long-pass filter LP467; AHF Analysentechnik) and was focussed onto the entrance slit of a spectrograph (SpectraPro 2150, Princeton, 300 grooves per millimetre, blaze wavelength 500 nm) equipped with a CCD camera (pco.pixelfly usb, PCO).

Correction of Bundle PL Spectra

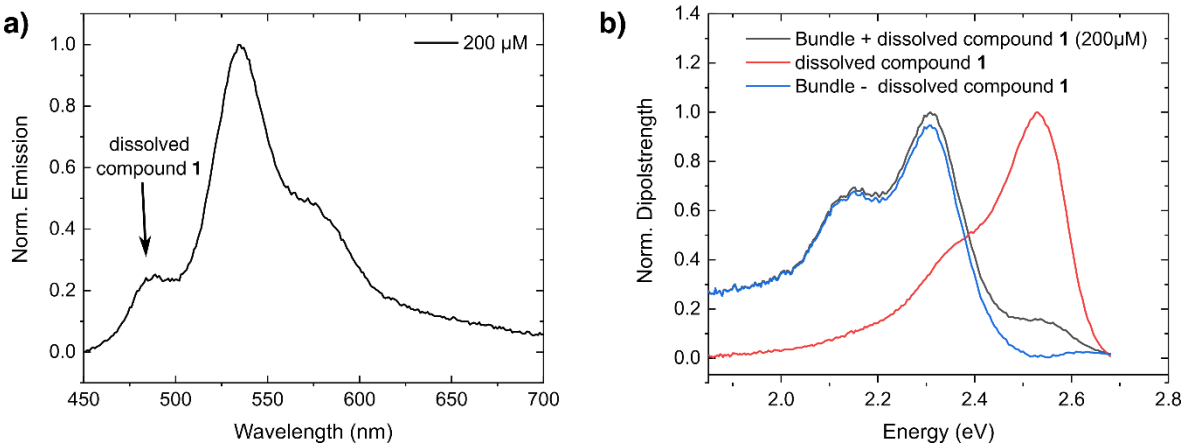

Fig. S7: Correction of the PL spectrum of compound 1 in anisole. a) Raw PL-spectrum of compound **1** in anisole at a concentration of 200 µM at room temperature. The peak at 490 nm stems from molecularly dissolved compound **1** in the dispersion due to some degree of remaining solubility. The stronger signal at longer wavelengths (> 510 nm) corresponds to PL from bundles of nanofibres. **b)** To obtain exclusively the PL spectrum of bundles (without monomer contribution), we converted the PL spectrum to an energy scale $I_{PL}(E)$ and to dipole strength via $I_{DP}(E) \propto I_{PL}(E)/E^3$, black curve. We then subtracted a converted, scaled and slightly shifted (0.01 eV) molecularly dissolved spectrum of compound **1** (red curve) from the measured and converted PL. The blue curve shows the resulting dipole strength of bundles of nanofibres.

Excited-State Lifetimes, Radiative Rates and PL Quantum Yields (PL-QY)

The PL decay was recorded by time-correlated single-photon counting (Fig. S8). For bundles an additional long-pass filter LP545 (AHF Analysentechnik) was used to suppress the monomer emission. The PL decay of dissolved compound **1** (THF) shows an exponential behaviour, see table S2.

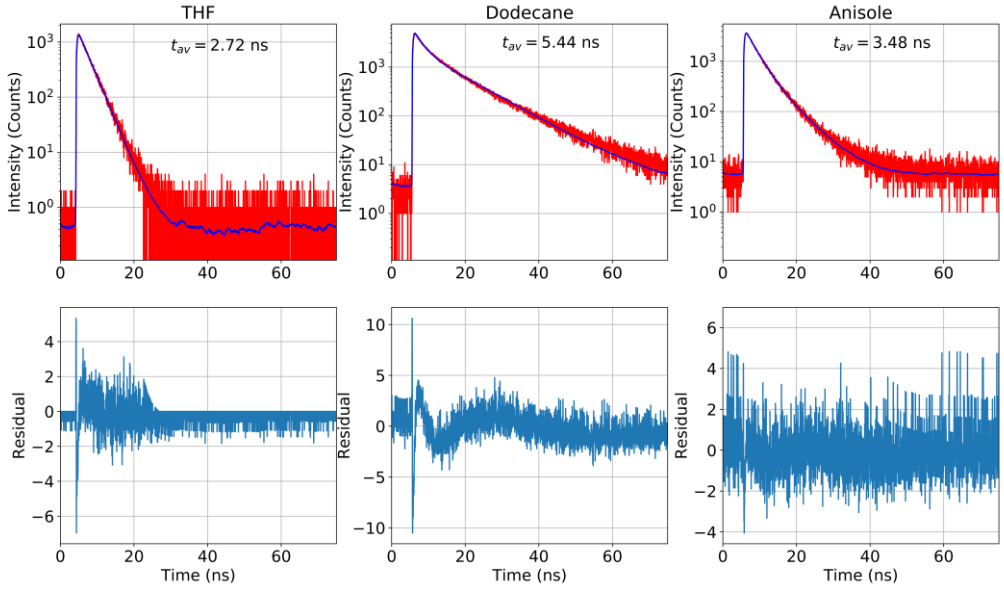

Fig. S8: PL-lifetime measurements. Left: Molecularly dissolved compound **1** in THF, middle: Single nanofibres in n-dodecane, right: Bundles of nanofibres in anisole. Top row: Time-correlated single-photon counting data (red) with fit function (blue). Bottom row: Weighted residuals. For all measurements, the concentration was 40 µM.

For both single supramolecular nanofibres (in n-dodecane) and for bundles of nanofibres (anisole) we found a bi-exponential PL decay with time constants t_i (relative amplitudes F_i) of $t_1 = 2.26\,ns$ ($F_1 = 3705.7$) and $t_2 = 10.45\,ns$ ($F_2 = 2353.59$), respectively $t_1 = 2.65\,ns$ ($F_1 = 3470.49$) and $t_2 = 5.97\,ns$ ($F_2 = 1144.86$). From these numbers we calculated the amplitude-averaged lifetime

$$t_{av} = \frac{\sum F_i t_i}{\sum F_i}. \qquad (8)$$

Tab. S2: PL-QY, excited-state lifetime and radiative lifetimes of (self-assembled) compound 1 in THF, n-dodecane and anisole (concentration: 40 µM).

	PL-QY	Excited state lifetime t_{av}	Radiative lifetime τ_r
THF	13.79 %	2.72 ns	19.72 ns
n-Dodecane	1.30 %	5.44 ns	418.46 ns
Anisole	2.58 %	3.48 ns	134.88 ns

5. Numerical Simulations of Experimental Spectra

To determine the electronic Coulomb coupling J_0 between the CBT-cores, the electronic disorder σ and the correlation length l_0 along the columns (single nanofibres as well as in bundles), we simulated the optical spectra of self-assembled compound **1** based on the numerical solution of a disordered Holstein Hamiltonian [6–9] and a residual analysis between simulation and data (Fig. 3B,C). The size of each nanofibre was limited for most of the cases to N = 20 CBT-cores for two reasons: First, this reduces the computational effort if combined with a truncation of the two-particle basis set (i.e., the position of the vibrationally excited molecule with respect to the vibronically excited molecule, see Fig. S5a; e.g. CutOff = 3: the vibrationally excited molecule sits at most three units away). Second, the 0-0 PL intensity is almost independent of N [9] and for N > 20 the absorption spectra remain unchanged [6]. Finally, we shifted the calculated spectra in energy to fit the measurements, which accounts for the (unknown) change of non-resonant dispersive interactions [8] when going from molecularly dissolved compound **1** to self-assembled compound **1**.

Usually, absorption spectra are used to determine the exciton bandwidth $W = 4J_0$. Unfortunately, our broad absorption spectra (Fig. 3B,C) made an unambiguous retrieval of all parameters (σ, J_0, l_0) impossible. We started therefore with the PL spectrum of isolated supramolecular nanofibres with its unique feature - the largely suppressed 0-0 peak intensity (Fig. 3B), which is approximately a function of $(l_0, \frac{\sigma}{W})$ [9]. We obtained then a *lower bound* for W for a maximised correlation length, i.e., $l_0 = \infty$ (see below for details). Based on these values for W the parameters W, σ and l_0 were further refined to reproduce all measured spectra of the different supramolecular morphologies. We exploited that the electronic Coulomb coupling J_0 (and thus the exciton bandwidth W) must be very similar in both isolated nanofibres and bundles of nanofibres, because the $\pi - \pi$-distance between CBT-cores (Fig. 2), the absorption spectra (Fig. 3B,C) as well as the circular dichroism spectra (Fig. S4) are almost identical for both morphologies.

Overall, we were able to reproduce the experimental spectra in Fig. 3 with good agreement using the following set of parameters:

$$
\begin{aligned}
W &\approx 4.3\, S\omega_0\,, \\
\sigma &\approx 0.85\, \omega_0, \\
l_0 &\approx 10 \qquad \text{for single nanofibres in n-dodecane,} \\
l_0 &\approx 0 \qquad \text{for bundles of nanofibres in anisole.}
\end{aligned}
$$

The parameters $S = 0.54$ and $\omega_0 = 0.157$ were determined by a Franck-Condon analysis of the PL and absorption spectra of molecularly dissolved compound **1** in THF (see Tab. S1).

Simulation of the PL of isolated nanofibres:

We varied W within the interval $W = S\omega_0\,[2, 2.5, \ldots, 6]$ to reproduce the suppressed 0-0 PL peak of the isolated nanofibres, and the energy disorder σ within the interval $\sigma = \omega_0[0.75, 0{,}8, \ldots, 1.05\,]$ to reproduce the linewidth. Smaller values of W did not describe the suppressed 0-0 PL intensity of isolated nanofibres at room temperature. For a correlation length of $l_0 = \infty$ the smallest residual for a truncation CutOff = 3 was obtained for $W = 5.5\ \omega_0\ S$ and $\sigma = 0.85\ \omega_0$ (Fig. S9a and black dashed curve in Fig. 3B). Also a more accurate calculation with a truncation of CutOff = 6 (Fig. S9b) led to nearly identical results, and the residuals ran

into a minimum for $W \geq 4.0\ \omega_0 S$ and $0.80\ \omega_0 \leq \sigma \leq 0.90\ \omega_0$. Note that *the values for W represent lower bounds*, because the correlation length was maximised.

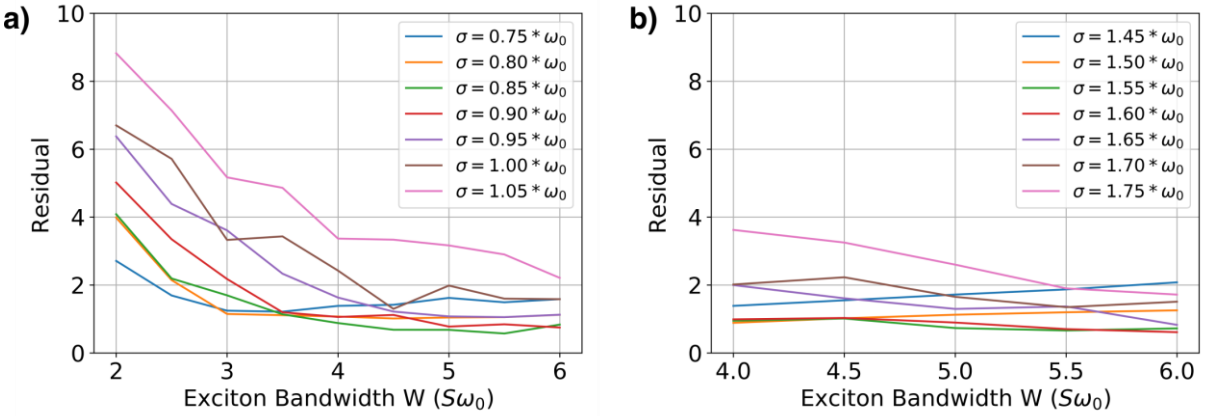

Figure S9: Residual analysis for the PL-spectrum of isolated nanofibres. a) Residuals for a calculation with truncation of CutOff = 3. b) Residuals for a calculation with a truncation of CutOff = 6**.**

Simulation of the absorption of isolated nanofibres and bundles of nanofibres:
Since the absorption depends only weakly on l_0 (because σ is of the order of W [10]), we also set $l_0 = \infty$ for the simulation of the absorption spectra and performed a residual analysis for W and σ. To be consistent with the simulation of the PL we limit the intervals to $W = S\omega_0\ [4, 4.1, \ \ldots, 5.5]$ and $\sigma = \omega_0 [0.75, 0.76, \ldots, 0.85\ ]$. For both single nanofibres and bundles the smallest residual was obtained for $W = 4.3\ \omega_0\ S$ and $\sigma = 0.84\ \omega_0$, see Fig. 3B,C (black lines).

Simulation of the PL of bundles of nanofibres:
Here, the challenge was to reproduce a "monomer-like" PL spectrum with a relatively large value of $W = 4.3\ \omega_0\ S$ for the exciton bandwidth. We took two steps: (i) We increased the disorder within the nanofibres in bundles by setting $l_0 = 0$, and (ii) we increased the number of monomers to N = 60 to increase the probability of finding monomers with site energies in the bottom tail of the Gaussian inhomogeneous distribution. For computational reasons, we chose a truncation of CutOff = 1. The PL spectrum in anisole, in particular the pronounced 0-0 PL intensity, can then be reproduced with the parameters $W = 4.3\ \omega_0\ S$ and $\sigma = 0.8$. Note, in order to get a good fit for higher values of σ, i.e. $\sigma = 0.85\ \omega_0$, the size of the nanofibres N have to be increased further. Importantly, a heavy-tailed Levy-type disorder [11] is not required to produce "monomer-type" PL spectra from molecular aggregates.

Coherence length* $\mathbf{N_{coh}}$ *for nanofibres and bundles of nanofibres:

Finally, we refined the value of l_0 to obtain an estimate for the coherence length N_{coh} in isolated nanofibres in n-dodecane. We chose the values determined above for $W = 4.3\ \omega_0\ S$ and $\sigma = 0.85\ \omega_0$ and performed a residual analysis for the PL spectrum with respect to l_0. To describe the suppresses 0-0 PL peak we restricted the spectral region to 486 nm - 600 nm (Fig. S10a). Furthermore, we used N = 40 monomers per nanofibre to minimize boundary effects and a truncation of CutOff = 3 to minimize computational efforts. From the best fit we found that $l_0 \approx 10$ CBT-cores, which leads to the coherence number $N_{coh} = 5.44$ CBT-cores (Fig. S10 b). Note, that as a consequence of our underestimated value for the coupling, this correlation length and coherence number itself is *a lower limit only*.

We obtained a coherence number for the bundles of $N_{coh} = 2.94$ CBT-cores, using $W = 4.3\ \omega_0\ S$; $\sigma = 0.85\ \omega_0$; $l_0 = 0$ and $N = 60$ CBT-cores from the simulation of the of the bundle PL (see above). Note, that this coherence number decreases with increasing N.

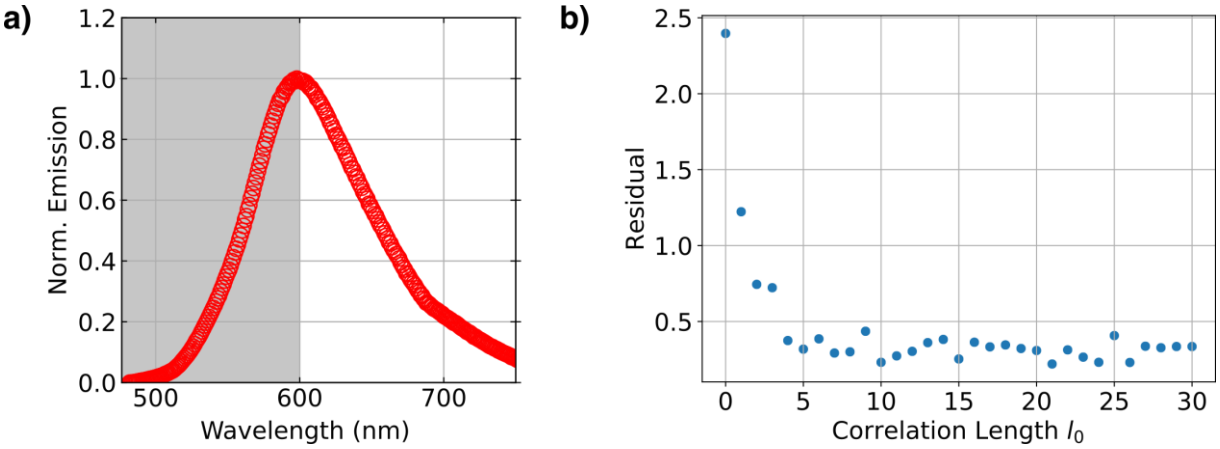

Figure S10: Coherence length in isolated nanofibres. a) PL spectrum of single supramolecular nanofibres in n-dodecane. The area highlighted in grey indicates the spectral region used for the residual analysis. **b)** Results of the residual analysis for the area highlighted in grey in a). The correlation length is given in units of CBT-cores along a nanofibre.

6. Experimental Setup

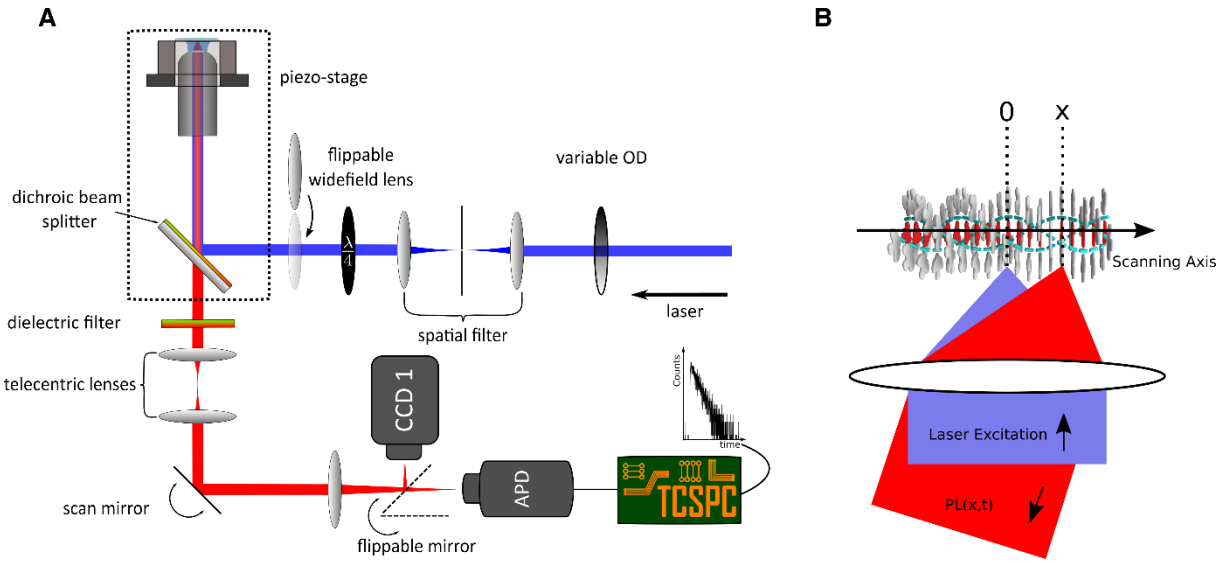

Fig S11: Experimental Setup. A) Optical setup with detection-beam scanning capabilities. For details, see 1. Materials and Methods. **B)** Schematic illustration of detection-beam scanning [modified, [12]]. During the entire detection-beam scan, the confocal excitation spot remains at the same position of the nanostructure, while the detection position imaged onto the APD is independently moved with the scan mirror.

To characterise the setup in Fig. S11, we used agglomerated SiOx-nanobeads (Corpuscular, diameter 52 nm), because energy transport between the nanobeads is negligible and a time-dependent broadening of the PL profile is not expected. Fig. S12 displays the results of detection-beam scanning on these nanobeads.

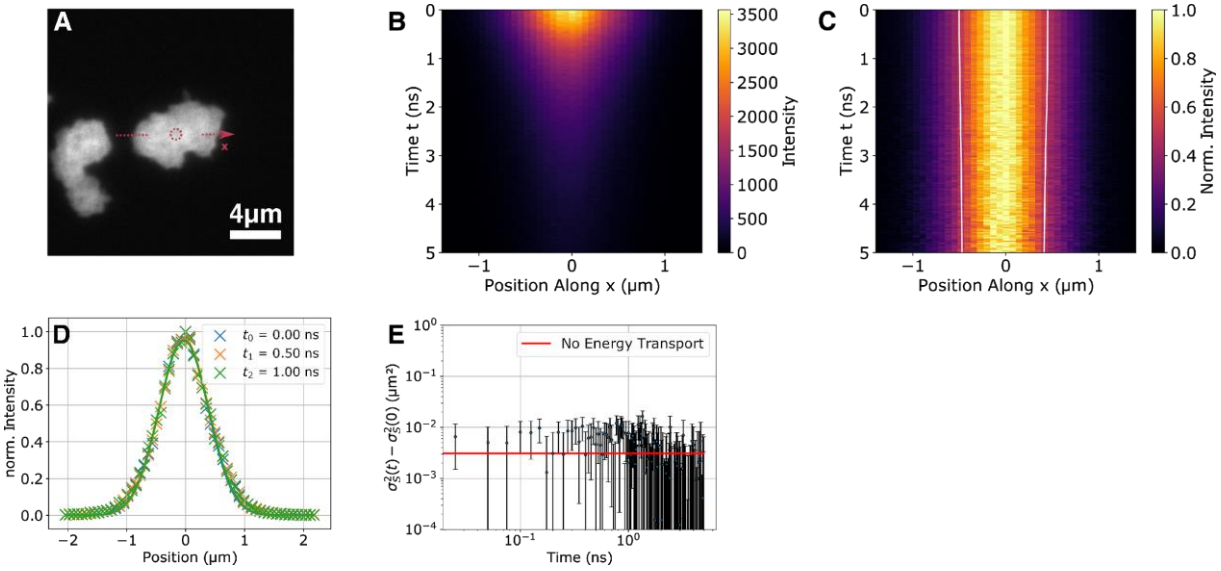

Fig. S12: Control experiment. A) Widefield PL image of agglomerated SiOx-nanobeads. The dashed red circle and arrow illustrate the position of confocal excitation and the direction of the detection scanning (x-axis), respectively. **B)** Spatio-temporal PL intensity distribution $I(x,t)$. **C)** Normalized PL intensity distribution as it evolves in space and time, measured along the axis illustrated by the red dashed arrow in A). The position x denotes the distance relative to the excitation position (x=0) along the arrow in A), and t = 0 ns corresponds to the arrival time of the excitation pulse. To emphasize changes in the width of the distribution, it is normalized at each time step. The contour lines indicate the time evolution of the full width at half maximum. **D)** Illustration of the normalized spatial intensity distribution $I(x,t_i)$ for three times t_i and the corresponding Gaussian fits, yielding e.g. a standard deviation of $\sigma_I\,(t=0) = 411\,nm$. Note that this number is determined by the convolution of the Gaussian excitation profile, the detection point-spread function and the detector chip size. **E)** Temporal changes of the second moments of the singlet excitons, revealing no resolvable energy transport in agglomerated SiOx-nanobeads.

7. Incoherent Exciton Diffusion Model

The extended diffusion equation for 1-dimensional incoherent transport with an exponential decay of the excitations reads [13–15]

$$\frac{\partial n(x,t)}{\partial (t)} = D(t)\frac{\partial^2 n(x,t)}{\partial x^2} - kn(x,t), \qquad (9)$$

where $n(x,t)$ is the exciton distribution that depends on both space and time. $D(t)$ is the time-dependent diffusivity that is related to an exciton hopping coefficient A by $D(t) = \frac{1}{2}A_\alpha t^{\alpha-1}$ with fractional time units for A [16]. Finally, k is the constant exciton decay rate.

Superdiffusive transport is characterized by $\alpha > 1$. For normal diffusion, $\alpha = 1$, the diffusivity $D = \frac{1}{2}A$ is time independent with units of cm^2s^{-1}. Subdiffusion is characterized by $\alpha < 1$ and occurs for exciton motion in a disordered excited-state energy landscape [17,18].

In our experiments the diffraction-limited confocal excitation spot creates to a good approximation an exciton population with a Gaussian profile and a standard deviation of σ. The solution to equation (9) is given then

$$n(x,t) \propto exp\left(-\frac{x^2}{2\sigma^2+2At^\alpha}\right) exp\,(-k\,t)\,. \qquad (10)$$

Note that the exponential decay ($exp\,(-kt)$) for the exciton population in equation (10) only changes the magnitude of this distribution at any point in time (and not its shape) and vanishes upon normalization to its maximum value at a given time, see Fig. 4C,D.

Equation (10) shows that the variance of the exciton distribution, which is also called the mean square displacement MSD $\langle x(t)^2\rangle$, evolves in time as [13,14]

$$\langle x(t)^2\rangle = \sigma_n^2(t) = \sigma^2 + At^\alpha, \qquad (11)$$

In a general situation with electronic disorder in the excited-state energy landscape the time-dependent diffusivity $D(t) = \frac{1}{2}A_\alpha t^{\alpha-1}$ decreases with time [15,16] (Fig. S14).

For normal diffusion ($\alpha = 1$), equation (12) transforms to

$$\langle x(t)^2\rangle = \sigma_n^2(t) = \sigma^2 + 2Dt. \qquad (12)$$

In general, the measured spatial intensity distribution (e.g. Fig. 4C,D) is a convolution of the exciton distribution $n(x,t)$, the detection point spread function $PSF(x)$ and the function of the APD detector size $C(x)$

$$I(x,t) = n(x,t) * PSF(x) * C(x). \qquad (13)$$

The PSF can be well approximated by a Gaussian function. The APD detector size is 50 µm and if the magnification of the setup of 83.9 is considered, the convolution of the PSF and the APD function can be well approximated with a Gaussian function with a time-independent variance σ_{setup} (see above Fig. S12). Therefore, the variance of the resulting Gaussian function is

$$\sigma_I^2(t) = \sigma_n^2(t) + \sigma_{setup}^2. \qquad (14)$$

The temporal changes in the variance of the spatial intensity distributions, i.e., the changes in the MSD, are calculated using the difference of the Gaussian variance (Eq. (14)) at a time t and the Gaussian variance at a fixed reference time $t = 0$. Using Eq. (11), the changes in the MSD due to diffusion with a Gaussian initial condition is then given by [13,14]

$$\Delta MSD = \sigma_I^2(t) - \sigma_I^2(0) = At^{\alpha}. \qquad (15)$$

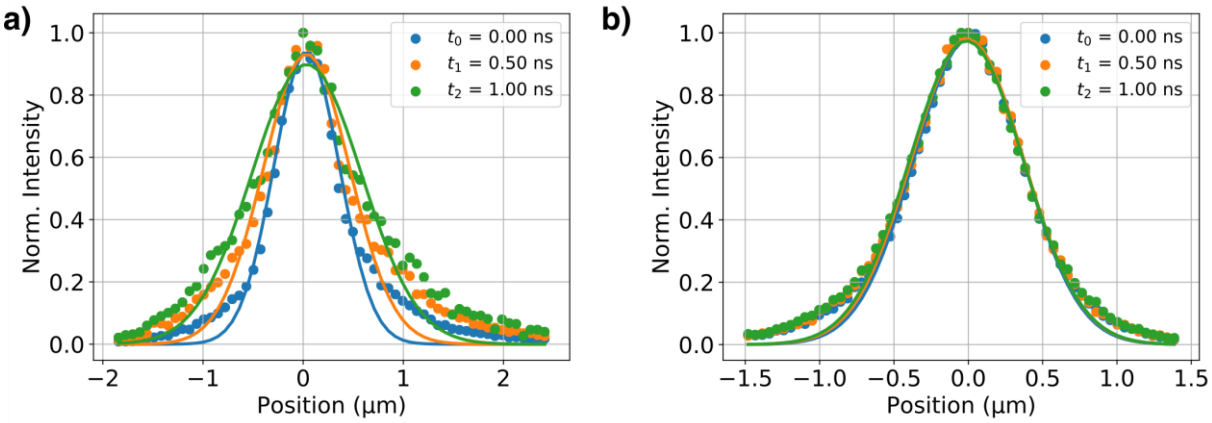

Fig. S13: Normalized spatial intensity distributions. a,b) Profiles from the normalized spatial intensity distributions $I(x, t_i)$ for the single nanofibre and the bundle of nanofibres, respectively, shown in Fig. 4C,D. The profiles were extracted at three times t_i and the solid lines show fits with Gaussian functions.

Fig. S13a,b show three profiles from the normalised spatial intensity distributions in Fig. 4C,D at different times. While Gaussian fits can roughly reproduce the intensity distribution of bundles, the profiles for the single nanofibre are very clearly non-Gaussian. This observation is related to the fact that each single nanofibre possesses its own unique excited-state energy landscape, which we directly probe in our single nanofibre experiment. In other words, we do not perform an ensemble average, and thus do not average out the specifics of each individual system. Thus, $n(x, t)$ does not evolve in time according to a Gaussian function.

To account for the non-Gaussian profiles, we evaluated the changes of the second moments (a measure for the widths) of our spatial intensity distributions, i.e.,

$$\Delta\mu_2(t) = \mu_2(t = 0) - \mu_2(t) = At^{\alpha}. \qquad (16)$$

For our spatial intensity distribution $I(x, t)$ the second moment at each point in time is defined as

$$\mu_2 = \frac{1}{N} \int (x - \mu_1)^2 I(x, t) dx \qquad (17)$$

where $N = \int I(x, t) dx$ is the integrated PL intensity and $\mu_1(t) = \frac{1}{N} \int xI(x, t) dx$ is the corresponding first moment (i.e., a measure for the centre of mass of the profile).

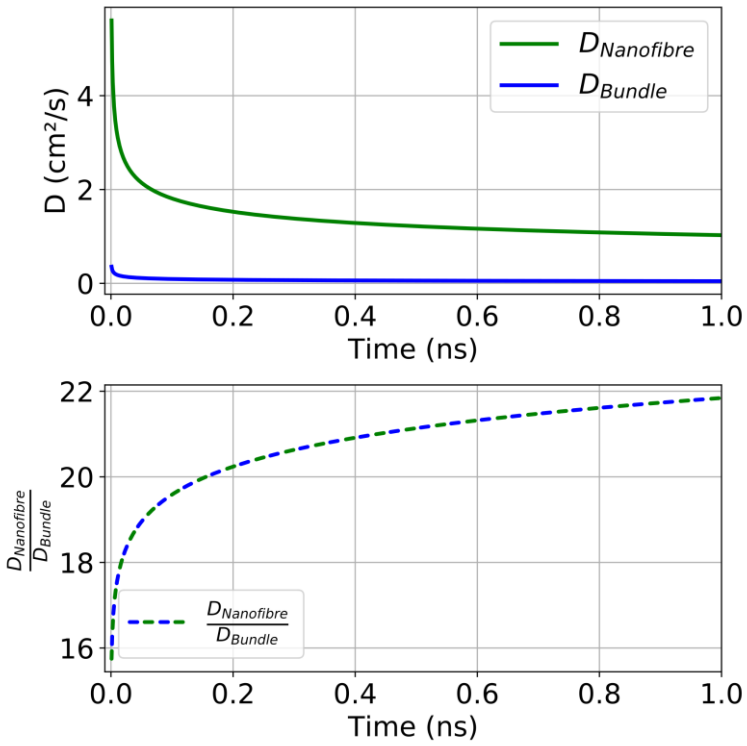

Fig. S14: Time-dependent diffusivities. Time-dependent diffusivity *D* of the single supramolecular nanofibre (green) and bundle (blue) shown in Fig. 4A,B.

8. References

(1) Haedler, A. T.; Meskers, S. C. J.; Zha, R. H.; Kivala, M.; Schmidt, H. W.; Meijer, E. W. Pathway Complexity in the Enantioselective Self-Assembly of Functional Carbonyl-Bridged Triarylamine Trisamides. *J. Am. Chem. Soc.* **2016**, *138* (33), 10539–10545. https://doi.org/10.1021/jacs.6b05184.

(2) Haedler, A. T.; Kreger, K.; Issac, A.; Wittmann, B.; Kivala, M.; Hammer, N.; Köhler, J.; Schmidt, H. W.; Hildner, R. Long-Range Energy Transport in Single Supramolecular Nanofibres at Room Temperature. *Nature* **2015**, *523* (7559), 196–199. https://doi.org/10.1038/nature14570.

(3) Eisele, D. M.; Knoester, J.; Kirstein, S.; Rabe, J. P.; Vanden Bout, D. A. Uniform Exciton Fluorescence from Individual Molecular Nanotubes Immobilized on Solid Substrates. *Nat. Nanotechnol.* **2009**, *4* (10), 658–663. https://doi.org/10.1038/nnano.2009.227.

(4) Zhang, W.; Jin, W.; Fukushima, T.; Saeki, A.; Seki, S.; Aida, T. Supramolecular Linear Heterojunction Composed of Graphite-like Semiconducting Nanotubular Segments. *Science* **2011**, *334* (6054), 340–343. https://doi.org/10.1126/science.1210369.

(5) Köhler, A.; Bässler, H. *Electronic Processes in Organic Semicond*uctors: An Introduction*. Wiley-VCH*; 2015.

(6) Spano, F. C.; Meskers, S. C. J.; Hennebicq, E.; Beljonne, D. Probing Excitation Delocalization in Supramolecular Chiral Stacks by Means of Circularly Polarized Light: Experiment and Modeling. *J. Am. Chem. Soc.* **2007**, *129* (22), 7044–7054. https://doi.org/10.1021/ja067321g.

(7) Hestand, N. J.; Spano, F. C. Expanded Theory of H- and J-Molecular Aggregates: The Effects of Vibronic Coupling and Intermolecular Charge Transfer. *Chem. Rev.* **2018**, *118* (15), 7069–7163. https://doi.org/10.1021/acs.chemrev.7b00581.

(8) Spano, F. C. The Spectral Signatures of Frenkel Polarons in H- and J-Aggregates. *Acc. Chem. Res.* **2010**, *43* (3), 429–439. https://doi.org/10.1021/ar900233v.

(9) Spano, F. C.; Clark, J.; Silva, C.; Friend, R. H. Determining Exciton Coherence from the Photoluminescence Spectral Line Shape in Poly(3-Hexylthiophene) Thin Films. *J. Chem. Phys.* **2009**, *130* (7), 074904. https://doi.org/10.1063/1.3076079.

(10) Clark, J.; Silva, C.; Friend, R. H.; Spano, F. C. Role of Intermolecular Coupling in the Photophysics of Disordered Organic Semiconductors: Aggregate Emission in Regioregular Polythiophene. *Phys. Rev. Lett.* **2007**, *98* (20), 206406. https://doi.org/10.1103/PhysRevLett.98.206406.

(11) Merdasa, A.; Jiménez, Á. J.; Camacho, R.; Meyer, M.; Würthner, F.; Scheblykin, I. G. Single Lévy States-Disorder Induced Energy Funnels in Molecular Aggregates. *Nano Lett.* **2014**, *14* (12), 6774–6781. https://doi.org/10.1021/nl5021188.

(12) Ciesielski, R.; Schäfer, F.; Hartmann, N. F.; Giesbrecht, N.; Bein, T.; Docampo, P.; Hartschuh, A. Grain Boundaries Act as Solid Walls for Charge Carrier Diffusion in Large Crystal MAPI Thin Films. *ACS Appl. Mater. Interfaces* **2018**, *10* (9), 7974–7981. https://doi.org/10.1021/acsami.7b17938.

(13) Clark, K. A.; Krueger, E. L.; Vanden Bout, D. A. Direct Measurement of Energy Migration in Supramolecular Carbocyanine Dye Nanotubes. *J. Phys. Chem. Lett.* **2014**, *5* (13), 2274–2282. https://doi.org/10.1021/jz500634f.

(14) Akselrod, G. M.; Deotare, P. B.; Thompson, N. J.; Lee, J.; Tisdale, W. A.; Baldo, M. A.; Menon, V. M.; Bulovic, V. Visualization of Exciton Transport in Ordered and Disordered Molecular

Solids. *Nat. Commun.* **2014**, *5* (1), 3646. https://doi.org/10.1038/ncomms4646.

(15) Akselrod, G. M.; Prins, F.; Poulikakos, L. V.; Lee, E. M. Y.; Weidman, M. C.; Mork, A. J.; Willard, A. P.; Bulović, V.; Tisdale, W. A. Subdiffusive Exciton Transport in Quantum Dot Solids. *Nano Lett.* **2014**, *14* (6), 3556–3562. https://doi.org/10.1021/nl501190s.

(16) Wu, J.; Berland, K. M. Propagators and Time-Dependent Diffusion Coefficients for Anomalous Diffusion. *Biophys. J.* **2008**, *95* (4), 2049–2052. https://doi.org/10.1529/biophysj.107.121608.

(17) Havlin, S.; Ben-Avraham, D. Diffusion in Disordered Media. *Adv. Phys.* **2002**, *51* (1), 187–292. https://doi.org/10.1080/00018730110116353.

(18) Vlaming, S. M.; Malyshev, V. A.; Eisfeld, A.; Knoester, J. Subdiffusive Exciton Motion in Systems with Heavy-Tailed Disorder. *J. Chem. Phys.* **2013**, *138* (21), 214316. https://doi.org/10.1063/1.4808155.